# Structural Disorder and Coherence across the Phase Transitions of Lead-Free Piezoelectric $Bi_{0.5}K_{0.5}TiO_3$

Bo Jiang[1], Trygve M. Raeder[1], De-Ye Lin[2], Tor Grande[1] and Sverre M. Selbach[1*]

[1]Department of Materials Science and Engineering,

NTNU – Norwegian University of Science and Technology, 7491 Trondheim, Norway.

[2]CAEP software Center for High Performance Numerical Simulation, Institute of Applied Physics and Computational Mathematics, Huayuan road 6, Beijing 100088, P.R. China

*Correspondence should be addressed to selbach@ntnu.no

Relaxor ferroelectrics exhibit superior properties for converting mechanical energy into electrical, and vice versa, but the structural disorder hampers an understanding of structure-property relationships, and impedes rational design of new, lead-free materials. $Bi_{0.5}K_{0.5}TiO_3$ (BKT) is a prototypical lead-free relaxor ferroelectric, but the microscopic origins of polarization, nature of the ferroelectric transition ($T_C$) and structural changes across the tetragonal to pseudo-cubic transition ($T_2$) are poorly understood. Here the local and intermediate structure of BKT is studied from room temperature to above $T_C$ by pair distribution functions (PDF) from synchrotron X-ray total scattering experiments and complemented by *ab initio* molecular dynamics (AIMD) simulations. The local structure varies smoothly across $T_2$ as well as $T_C$, in contrast to the abrupt changes at $T_C$ inferred from conventional diffraction. Ferroelectric distortions are larger on the local scale than in the average structure, with polar $Ti^{4+}$ displacements prevailing above $T_C$. We find that local polar regions partly cancel each other below $T_C$, while completely averaging out above, implying that BKT goes through a transition from partial to complete disorder across $T_C$.

## 1. Introduction

Bismuth potassium/sodium titanate, $Bi_{0.5}K_{0.5}TiO_3$ (BKT) and $Bi_{0.5}Na_{0.5}TiO_3$ (BNT) are lead-free piezoelectric perovskites [1-3] which are important end members in solid solutions which can replace environmentally hazardous $Pb(Zr,Ti)O_3$ (PZT) [3, 4]. Bismuth based PZT replacements also possess $6s^2$ lone pairs which play an important role in the spontaneous polarization and structural distortion [5, 6]. BKT was first reported in 1961 [7], and solid solutions based on BKT have shown promising piezoelectric and ferroelectric properties [8-15]. Compared to rhombohedral *R*3*c* BNT, BKT is comparatively less studied, partly due to challenges with sintering dense polycrystals, and to pole these materials [9, 16-18]. The structure of ferroelectric BKT is tetragonal *P*4*mm* (a = 3.933 Å, c=3.975 Å, c/a=1.01[17]) below the second-phase transition temperature [3, 16, 18-20] $T_2$ of 270-310 °C, pseudo-cubic above $T_2$, and finally paraelectric cubic $Pm\overline{3}m$ above the Curie temperature $T_C$ of 370-410 °C [3, 16, 18, 21, 22].

BKT ceramics show relaxor-like behavior with broad dielectric peaks which have frequency dependent temperatures of maximum permittivity [23-25]. Polar nanoregions (PNR) characteristic of relaxors emerge below the Burns temperature $T_D$ [19, 26], and the correlation length and volume fraction of PNR increases upon further cooling. PNR have lower symmetry than the average structure, but as they only extend over a few lattice constants they are difficult to detect by conventional reciprocal space diffraction [28]. A recent study of the local crystal and domain structures of BKT [22] reported polar domains at low temperature and a binary stability field in which cubic and tetragonal phases coexist between $T_2$ and $T_C$. Coexistence of ferroelectric domains and PNR was also found in a study of the grain size dependence of the phase transitions of BKT [23, 29], indicating coexistence of ferroelectric domains and PNR.

The local structure and relaxor-like behavior in BKT may also be influenced by A-site cation ordering. In perovskites B-site cation ordering is known to be favored when there is a large difference in cation size and charge, while A-site cation ordering is less common [30, 31]. In BKT the mixed A-site cation sublattice is disordered with no superstructure peaks with cation

ordering observed, although $Bi^{3+}$ (1.31 Å) and $K^{+}$ (1.65 Å)[32] differ in radii by 21% and in formal charge. In our previous work on the local structure of BKT we found several local A-site cation orders to be degenerate from 0K DFT calculations, hence no single cation ordering pattern is favored [33]. Pair distribution functions (PDF) from total scattering (synchrotron X-rays or neutron) can probe the local and intermediate range structure of amorphous and disordered materials [34-37]. Total scattering can be performed over a wide range of temperatures, or with variation of other thermodynamic parameters, like e.g. electric field, which was recently used by Liu *et al.* to study polarization rotation in ferroelectric perovskites [38, 39]. Compared to neutrons, which are more sensitive to light elements, but strongly absorbed by some elements and negatively scattered by others, synchrotron X-rays have the advantages of rapid data collection even with small samples. Relaxor ferroelectrics with structural disorder benefits from PDF analysis as the local structure can be correlated with macroscopic properties [40-42], e.g. PNR were first directly observed by Jeong *et al.* using neutron PDF to characterize $Pb(Mg_{1/3}Nb_{2/3})O_3$ [43]. Modeling of the PDF can provide more realistic structural models for computational studies, and vice versa [33, 44, 45].

Here we report the temperature evolution of the local structure of $Bi_{0.5}K_{0.5}TiO_3$ (BKT) inferred from synchrotron X-ray pair distribution functions (PDF) and *ab initio* molecular dynamics (AIMD) simulations [46]. Experimental signatures of both tetragonal and cubic phases are found between $T_2$ and $T_C$, suggesting the presence of tetragonal PNR. While the ferroelectric transition at $T_C$ appears to be abrupt from reciprocal diffraction, PDFs demonstrate that the local structure changes smoothly across $T_C$. Finally, we propose a model for the thermal evolution of the structural disorder in BKT, supported by both AIMD and fitting of experimental PDFs to both crystallographic models and reverse Monte Carlo simulations.

## 2. Experimental and Computational Details

*Materials synthesis:* $Bi_{0.5}K_{0.5}TiO_3$ (BKT) powder was prepared as described in our previous work [33].

*Synchrotron X-ray total scattering and data analysis:* Synchrotron X-ray total scattering was performed at beamline ID22 (λ = 0.199965 Å, 62 keV) at the European Synchrotron Radiation Facility (ESRF). Powder mounted in spinning capillaries were measured in transmission mode with a 2D image plate detector (Perkin Elmer XRD 1611). Data were collected upon heating using a hot air blower. Rietveld refinement was done with the General Structure Analysis System (GSAS) [47] program. The PDF G(r) were obtained with PDFgetX3 [48] using a $Q_{max}$ of 22.8 $Å^{-1}$, and analyzed using PDFgui [49] and RMCprofile [50].

*Density functional theory:* Density functional theory (DFT) calculations were performed with the *Vienna Ab initio Simulation Package* (VASP) code [51, 52] using the PBEsol functional [53, 54]. The standard PBE PAW potentials Bi_d ($5d^{10}6s^26p^3$), K_sv ($3s^23p^654s^1$) Ti_pv ($3p^63d^24s^2$) and O ($2s^2p^4$) supplied with VASP were used. Supercells containing 40 atoms represented by 2×2×2 perovskite unit cells were used in this work. There are six different configurations of A-atoms for cubic structures for the 1:1 stoichiometric ratio of Bi and K in $Bi_{0.5}K_{0.5}TiO_3$ [33]. All the geometry optimized configurations are named according to convention introduced by Gröting and Albe [55, 56]. For ground state geometry optimization, the Brillouin zone integration was done on a 3×3×3 gamma centered k-point grid for the 2×2×2 $Bi_{0.5}K_{0.5}TiO_3$ supercell with 40 atoms and plane waves were expanded up to a cutoff energy of 550 eV. The Hellman-Feynman forces on the ions were relaxed until they were below 0.001 eV/Å.

*Ab initio* molecular dynamics (AIMD) simulations using the NVT ensemble [57] were carried out via the algorithm of Nosé [58] to control the temperature oscillations during the DFT calculations. Brillouin zone integration was done on a single gamma-centred k-point and the cut off energy was reduced to 400 eV for all AIMD calculations. We used a 4×4×4 disordered supercell $Bi_{32}K_{32}Ti_{64}O_{192}$ containing 320 atoms derived from RMC simulations as the starting model

before optimizing the geometry at 0K to obtain the initial structure for AIMD. Each AIMD simulation ran for least 5000 steps with a time-step of 1 fs. The last 3000 steps were used to generate the time averaged structure at each temperature. The spontaneous polarization $P_s$ for the disordered supercells were calculated by a point charge method.

## 3. Results and Discussion

### 3.1 Local and Intermediate Range Structure

X-ray patterns of the BKT powder from room temperature to 773 K in intervals of 50 K are displayed in Figure 1. Reciprocal space X-ray patterns of BKT powder from 298 to 773K are consistent with previous studies [22]. No impurity phase was detected at any temperature. The phase transition from ferroelectric tetragonal to the paraelectric cubic structure is evident from the split pseudocubic $(200)_c$ and $(210)_c$ Bragg reflections in Figure 1b and 1c, respectively, merging gradually upon heating. The room temperature asymmetry of the $(102)_t$ and $(201)_t$ reflections, due to tetragonal distortion, is still visible at 523 K, just below the $T_2$ of about 543 K. Results from Rietveld refinements using a mixed A-site *P*4*mm* model are summarized in Table S1.

To investigate the local structure of BKT, temperature dependent PDF G(r)s are analyzed. The low r region of the temperature dependent PDFs reveal the first coordination shells, as seen in Figure 2a-b. PDFs simulated for *P*4*mm*, pseudo-cubic and $Pm\bar{3}m$ structures with mixed A-site model are shown in Figure 2a, while the temperature dependent measured synchrotron X-ray PDFs are depicted in Figure 2b. The pseudo-cubic structure is based on the high-symmetry $Pm\bar{3}m$ structure, with small displacements of all ions and small changes applied to the lattice parameters to break the initial high symmetry before geometry optimization by DFT. The peaks

from 3 to 4 Å, corresponding to A-Ti (A = Bi, K), A-A and Ti-Ti bonds, vary significantly between the three different structure models in Figure 2a, but none of these models can reproduce the measured PDF, as shown in Figure 2b. The *P*4*mm* model gives double peaks for the A-Ti bonds, while in contrast the pseudo-cubic and $Pm\bar{3}m$ structures give broader, more subtle peaks between 3 and 4 Å.

The A-Ti, A-A and Ti-Ti bond distance peaks, highlighted by dotted lines in Figure 2b, show distinctly different pattern evolution with temperature. At room temperature, the first A-Ti peak is significantly higher than the second, but decreases rapidly with increasing temperature, signifying a rearrangement of the A-Ti bonds upon heating. The two A-Ti bond peaks do not merge to one peak at the highest temperature, which would correspond to an ideal cubic $Pm\bar{3}m$ structure, but remain separated at the highest measured temperature. This implies that not only do $Ti^{4+}$ displacements prevail into the high temperature cubic phase, but their magnitude remains almost unaffected upon heating. We thus infer that the average A-site mixed model gives a poor description of the local structure of BKT. The experimental PDF patterns show only subtle changes in the peak positions across the phase transition from tetragonal to cubic, but a large reduction in intensity. The deviation between the *P*4*mm* modeled PDF in the inset of Figure 2b and the measured PDF will be discussed in more detail below.

To examine the intermediate range structure of BKT, we extend the PDF patterns to r as high as 150 Å in Figure 2c-f. There are no abrupt or even significant changes in the 2-16 Å range in Figure 1c apart from the expected peak broadening due to increasing thermal vibrations upon heating. This indicates that the intermediate structure does not significantly change upon heating or across the phase transition from tetragonal to cubic phase. There is no unambiguous evidence of PNR in the PDFs for BKT, in contrast to previous investigations of PMN [43], but tetragonal PNR would be difficult to distinguish from the average *P*4*mm* structure. However, two additional peaks indicated by arrows in Figure 1d appear upon heating,

and can be assigned to the cubic high temperature phase. Above 40 Å we see a different thermal evolution than observed for the local structure. The peaks above 50 Å get sharper upon heating and this is more pronounced for higher r, corresponding to a more symmetric cubic phase, as can be seen in Figure 2e and f. The structural coherence length at about ~40 Å implies that an order-disorder-type phase transition from tetragonal to a cubic structure occurs upon heating, where local tetragonal regions cancel each other in an on average cubic structure. This resembles the order-disorder ferroelectric transitions in $BaTiO_3$ [59, 60].

The PDFs of BKT at different temperatures were first refined by small-box modeling with PDFgui [49], using mixed A-site *P*4*mm*, pseudo-cubic and $Pm\bar{3}m$ structure models. Isotropic *U* factors (atomic displacement parameters, ADP) from reciprocal space modeling are presented in Figure 3 (a-d). Table S2 summarizes the results from real space PDF refinements with space group *P*4*mm* in the r range of 1.5-80 Å from room temperature to 773K. ADPs encompass both thermal vibrations as well as local structural disorder at lattice sites, and anomalously large ADPs for certain atoms signify that the structural model used does not capture local displacements. The ADPs of Bi/K and Ti for the *P*4*mm* structure shows similar thermal evolution from PDF (Figure 3a) and Rietveld (Figure 3d), both having anomalously high values at room temperature with only subtle increase upon heating. This indicates that the structural disorder in the cation sublattices only increases subtly upon heating. For Bi/K the ADPs increase faster between $T_2$ and $T_C$ than at lower and higher temperatures. The same slope across $T_2$ can also be seen in Figure 3b for the Bi/K ADPs within the pseudo-cubic model, and in Figure 3c for the $Pm\bar{3}m$ model. Interestingly, the Ti ADPs from PDF modeling with pseudo-cubic and $Pm\bar{3}m$ models decrease across $T_2$, suggesting less structural disorder on the B-site sublattice above $T_2$ than below. Reciprocal space refinement does not capture the local structural changes, as seen from the small changes in the ADPs of Ti and O across $T_2$. The reliability factor $R_w$ in Figure 3e support that the local structure of BKT below $T_2$ is better described as tetragonal

*P*4*mm* than as pseudo-cubic or ideal cubic $Pm\overline{3}m$. Above $T_2$, $R_w$ for the *P*4*mm* model increases again, as shown in the inset of Figure 3e, while $R_w$ for the pseudo-cubic structure decreases strongly. The ideal cubic $Pm\overline{3}m$ model gives higher $R_w$ factors for all temperatures, but this is expected from the lower number of structural degrees of freedom compared to the *P*4*mm* and pseudo-cubic structures. A second infliction point for $R_w$ for *P*4*mm* in the inset of Figure 3e occurs at $T_C$. Compared to the evolution of $R_w$ for the pseudo-cubic model, the structure of BKT above $T_C$ is inferred to become gradually more ordered in line with the peak sharpening at high r in Figure 3 (c-d) in the main text. The increasing $R_w$ for the pseudo-cubic model above $T_C$ supports the ideal cubic $Pm\overline{3}m$ as the high temperature phase. Displacements of $Ti^{4+}$ along the z-axis ($z_{Ti}$) can be as used a measure of the local polarization in BKT, as shown in Figure 3f for different temperatures as a function of $r_{max}$ in the PDF refinements. For $r_{max}$ larger than ~40 Å the refined $z_{Ti}$ is insensitive to $r_{max}$, but decreases with increasing temperature, resembling the expected behaviour of a displacive phase transition. Below $r_{max}$ of ~40 Å $z_{Ti}$ increases rapidly with decreasing $r_{max}$, and as the refined $z_{Ti}$ is very similar for all temperatures for the smaller $r_{max}$ values. The increase in $z_{Ti}$ with decreasing $r_{max}$ is much stronger for high temperatures than low. Prevailing local displacements of Ti at high temperatures is consistent with the low *r* range PDFs presented in Figure 2. The close to constant value of $z_{Ti}$ above ~40 Å also suggests a structural coherence length about ~40 Å, fully in accordance with the intermediate range PDFs shown in Figure 2 (b-d) in the main text. The step-like shifts of $z_{Ti}$ in the low *r* range in Figure 3 coincides with the lattice periodicity.

The thermal evolution of the lattice parameters *a* and *c* and the tetragonality *c/a* from Rietveld refinement and small-box modeling of PDF are shown in Figure 4. Rietveld refinement and PDF refined for the *r* range 1.5 to 80 Å show very similar trends for *c* and *c*/*a*, but with a minor deviation for *a*. Note that the absolute values from Rietveld and PDFgui are not completely comparable due to systematic offset as these two methods probe different information

embedded in the same data sets. *c* systematically decreases when the *r* range is reduced from 80 Å to 30 Å, while *a* is less sensitive (Figure 4a and 4b). The same systematic trend can also be seen for the tetragonality *c/a* in Figure 4c, meaning that the local structure of BKT is more tetragonally distorted than the average structure. Particularly, *c*/*a* does not drop to, or even approach, unity upon crossing and heating beyond $T_C$. The refined lattice parameters from PDF also change more smoothly across $T_C$ than those obtained from Rietveld refinement. This indicates a diffuse phase transition on the local scale, compared to the apparent abrupt change in average structure. A similar phenomenon has been reported for $BaTiO_3$ nanoparticles [61-63], which also show diffuse ferroelectric phase transition for small particles. The diffuse transition across $T_C$ is inferred from the local and intermediate structure up to ~80 Å, in contrast with the abrupt change in average structure, suggest a low degree of structural coherence.

### 3.2. Reverse Monte Carlo Modelling

As small-box modelling using crystallographic models implicitly presumes long-range order, we now turn to large-box reverse Monte Carlo (RMC) simulations, which are not confined by space group symmetry and can thus better capture short range order. The total and partial PDFs for BKT at room temperature extracted from small-box modeling with PDFgui and large-box RMC modeling are shown in Figure 5a and b, respectively. For small-box modeling an average mixed A-site *P*4*mm* model was used, while RMC simulations were done with 12×12×12 supercell models with 8640 atoms. In the low r region in Figure 5a it is evident that the average structure model gives a poor fit to the experimental PDF, while the fit improves progressively with increasing *r* above 4 Å. In contrast, the RMC model gives an excellent fit to the experimental PDF over the whole considered *r* range as shown in Figure 5b. A series of high temperature PDF fitted by RMC are presented in Figure 5d together with the 12×12×12 BKT supercells folded into single unit cells to visualize the distribution of cation positions. RMC

simulated PDFs at all temperatures show excellent fit for the whole r-range. Nearest neighbor functions $n_{A\text{-}A}$(r) shown in Figure S1 indicate that the A-site sublattice with $Bi^{3+}$ and $K^{+}$ cations is completely disordered at all temperatures. At room temperature, all the cation clouds show large spheroidal distributions compared to an ordered crystalline oxide like $BiFeO_3$ [33], reflecting the large degree of positional disorder in BKT even at room temperature. The cation clouds increase gradually across $T_2$ at ~550 K, as seen from comparing the clouds at 473 K and 573 K in Figure 5d. Upon further heating above $T_2$ and crossing $T_C$ the cloud sizes increase only subtly. This behaviour is consistent with the thermal evolution of the ADPs, which also describe positional disorder, see Figure 3.

From the partial PDFs in Figure 5a we can see that the local structure difference between experimental and calculated PDFs mainly come from Bi-Ti bond distance peaks. There is a broad peak for Bi-Ti peaks containing two different Bi-Ti peaks because of the polar $Ti^{4+}$ displacements along the z-axis, as illustrated in fragment structure of Figure 5c. The K-Ti peaks contribute less due to the smaller X-ray scattering strength of $K^{+}$ compared to $Bi^{3+}$. This suggests that $Bi^{3+}$ displacements are the main source of local structure disorder, as also reported in an X-ray PDF study of BNT [34]. The partial PDFs from RMC simulations in Figure 5b are similar to those extracted from small-box modeling with PDFgui in Figure 5a, but the much larger model used for RMC allows more local structural distortions than an average structure small-box model. The peaks at 3.25, 3.65, 6.25 and 7.9 Å in the experimental PDF fit very well with the RMC derived model, in contrast with the small-box model with PDFgui. The peaks at 3.25 Å and 3.65 Å (see Figure 5b) show asymmetrical distributions of Bi-Ti bond distances, which is major source of fitting error with small-box fitting.

To examine the local bond environments upon heating BKT, the partial PDF of A-site (Bi/K)-Ti bond distance distributions at 300K (P*4mm*), 573K (pseudo-cubic) and 773K $Pm\bar{3}m$ are displayed in Figure 6. The dashed lines in Figure 6a denote the two different Bi-Ti bond

distances caused by displacements of $Ti^{4+}$ relative to $Bi^{3+}$ illustrated in Figure 6c. The peak heights of partial Bi-Ti PDFs at about 3.25 Å and 3.65 Å decrease with increasing temperature. The first (short) Bi-Ti peak decays faster than the second (long) Bi-Ti bond peak with increasing temperature, suggesting that the Bi-Ti bond distribution rearranges across the phase transitions at $T_2$ and $T_C$. It is noteworthy that these two peaks prevail at high temperature, in agreement with the analysis of $Ti^{4+}$ displacements in Figure 2a and b. In contrast, the K-Ti bond distance peaks in Figure 6b exhibit close to single Gaussian distributions about the mean position under different temperatures, and with subtly increasing peaks width upon heating. This suggests that displacements of $K^+$ are not the origin of local structural distortions in BKT.

There are ten different 2×2×2 perovskite supercell *P*4*mm* configurations of BKT, and the statistical distribution of A-site (Bi/K)-Ti bond lengths from DFT optimized structures are shown in the insets in Figures 6a and b. The Bi-Ti bond length distribution shows two distinct peaks while the K-Ti bond length distribution has only one peak, in accordance with the A-site (Bi/K)-Ti bond distances from RMC. From this, we propose two distinctly different local bond environments for Bi-Ti and K-Ti (Figure 6c), which is qualitatively similar to a previous report on BNT [34]. The $6s^2$ lone pair cation $Bi^{3+}$ is strongly displaced with respect to its nearest neighbor $Ti^{4+}$ cations, while $K^+$ is situated at the centre of its first $Ti^{4+}$ coordination shell.

### 3.3. *Ab initio* Molecular Dynamics Simulations

The PDF analysis of the synchrotron X-ray total scattering data provided information on the temperature evolution of local and average structure, especially correlations between the A and B cation sublattices. However, the details of the oxygen sublattice are not easily resolved by X-ray scattering, hence we use *ab initio* molecular dynamics (AIMD) simulations to complement the measurements. Relaxed structures for different configurations at 0K are shown in Figure 7a.

The relative shift between $Bi^{3+}$ and $K^{+}$ along the c-axis is caused by different charges and bond lengths towards oxygen [33]. AIMD simulations were performed with these six configurations in 4×4×4 disordered $Bi_{32}K_{32}Ti_{64}O_{192}$ supercells, and the polarization was calculated using a point charge model, see Figure 7b. At higher temperatures, supercells with disordered A-site sublattices show almost zero polarization compared to the remaining polarization in ordered configurations, implying that multiple local polar regions partly cancel each other. We note that the A-site, B-site and Ti-O octahedra become more distorted with rising temperature, as expected due to increasing thermal vibrations, as can be seen in Figure S2.

In order to analyze the Bi-Ti bond distribution in BKT at different temperatures, the first Bi-Ti asymmetric peak from 2.5Å to 4.5Å is deconvoluted into two equal area Gaussian peaks as shown in Figure 8a-d. These two peaks correspond to the long and short peaks for the relative displacement of Bi-Ti derived from the time averaged structure. After equilibration under different temperature, the average Bi-Ti peak still shows asymmetrical distributions at 1300K, which means that the $Ti^{4+}$ displacements relative to $Bi^{3+}$ in BKT also prevail into the high temperature phase from AIMD calculations. AIMD results for K-Ti bond distributions in Figure 8e and 8f show single Gaussian distributions, in agreement with experimental partial PDFs from RMC fitting (Figure 6).

A-site environment at different temperatures, presented as AIMD simulated partial PDFs for Bi-Bi, K-K, Bi-O and K-O, are shown in Figure 8g-j. The K-K bond distribution is mainly responsible for increasing disorder on A-sites upon heating, while the Bi-Bi bond distribution shows little change. The bond length distributions for the coordination polyhedra $(Bi/K)O_{12}$ from AIMD are shown in Figure 8i and 8j. There are three distinct peaks in the Bi-O bond distribution at 300K and 800K which are not present for K-O. Bi and K thus have distinctly different local environments at high temperatures, as also previously reported at room temperature [33].

Distortions of the $TiO_6$ octahedra contribute to the spontaneous polarization, but this is not easily captured by synchrotron PDF due to the lower X-ray scattering strength of $O^{2-}$. Figure 9 describes the distributions of $Ti^{4+}$ and $O^{2-}$ positions at 300K and 800K by time averaging structures from AIMD. There are distinct relative shifts between $Ti^{4+}$ and $O^{2-}$ centrosymmetric positions along all the directions in Figure 9a, corresponding to the tetragonal distortion of BKT at lower temperatures. AIMD simulations at room temperature support the reduced polarization due to local A-site cation ordering. As the temperature rises to 800K ($T_C$ ~650K), as seen in Figure 9b, the distribution peak widths for $Ti^{4+}$ and $O^2$ increases due to thermal vibrations, while the average position for $Ti^{4+}$ and $O^{2-}$ is the same along all axes. In paraelectric cubic BKT at high temperature, the $Ti^{4+}$ ions are located at the centre of the $TiO_6$ octahedra.

Based on the analysis of the presented results from synchrotron X-ray PDF and *ab initio* molecular dynamic (AIMD) at ambient and elevated temperatures, we propose that the phase transitions of BKT are strongly order–disorder, resembling $BaTiO_3$ [59, 60] and PZN-*x*PT [64]. The proposed schematic thermal evolution of the crystal structure is illustrated in Figure 10. Although no direct evidence of polar nanoregions (PNR) in BKT could be discerned from the PDFs, we can still consider the enhanced local tetragonal distortion as nanometer sized polar regions with larger local polarization. However, it would be challenging to unambiguously identify tetragonal PNR in an on average tetragonal lattice. At room temperature, the structure of BKT shows local tetragonal polar regions, and A-site disorder leads to local variations in the direction of the polarization, which leads to partial cancelling. As the temperature rises, the local structure remains essentially the same, but the average structure approaches pseudo- cubic and $Pm\bar{3}m$ structures, where local polar regions cancel each other completely. The $Ti^{4+}$ displacements remain close to constant from room temperature to high temperature. Future efforts to optimize the properties of BKT through cation substitution should correlate the thermal evolution of the local and intermediate structure with the dielectric permittivity and piezoelectric coefficients.

## 4. Conclusions

The temperature evolution of the local and average structure of BKT were investigated by synchrotron X-ray total scattering and *Ab initio* molecular dynamics simulations. The experimental pair distribution functions (PDF) were analyzed by small-box modeling with PDFgui and large-box RMC simulations. Rietveld refinements and PDF modeling demonstrated that between $T_C$ and $T_2$ he pseudo-cubic lattice can be interpreted as tetragonal PNR in a cubic matrix. While the average structure apparently changes abruptly, the phase transition across $T_C$ is diffuse and continuous on the local scale. Local $Ti^{4+}$ displacements are larger than inferred from the spatially averaged structure, and prevail into the high temperature cubic phase. A structural coherence length about ~40 Å was found from PDF analysis. Redistributions of the Bi-Ti bond lengths constitute the major structural distortions in BKT upon heating, while the distinctly different K-Ti local environment does not change significantly from low to high temperature. We suggest a structural model of BKT where multiple local tetragonal polar regions exist at room temperature, while upon heating these local polar regions increasingly cancel each other, rendering BKT on average cubic and paraelectric above $T_C$.

## Supporting Information

Additional experimental and computational details, results from Rietveld and PDFGUI refinements, analysis of thermal evolution A-site ordering and additional results from ab initio molecular dynamics simulations.

## Acknowledgements

This work was supported by the Research Council of Norway through the SYNKNØYT project 228571. Computational resources were provided by Uninett Sigma2 through the project NN9264K. We thank Andrew Fitch for his valuable assistance at beamline ID22 at ESRF.

## References

(1) Kitanaka, Y.; Yanai, K.; Noguchi, Y.; Miyayama, M.; Kagawa, Y.; Moriyoshi, C.; Kuroiwa, Y., Non-180° polarization rotation of ferroelectric $(Bi_{0.5}N_{0.5})TiO_3$ single crystals under electric field. *Phys. Rev. B* **2014,** *89*, 104104.

(2) Isupov, V. A., Ferroelectric $Na_{0.5}Bi_{0.5}TiO_3$ and $K_{0.5}Bi_{0.5}TiO_3$ perovskites and their solid solutions. *Ferroelectrics* **2005,** *315*, 123-147.

(3) Rödel, J.; Jo, W.; Seifert, K. T. P.; Anton, E. M.; Granzow, T.; Damjanovic, D., Perspective on the development of lead-free piezoceramics. *J. Am. Ceram. Soc.* **2009,** *92*, 1153-1177.

(4) Shvartsman, V. V.; Lupascu, D. C., Lead-Free Relaxor Ferroelectrics. *J. Am. Ceram. Soc.* **2012,** *95*, 1-26.

(5) Schutz, D.; Deluca, M.; Krauss, W.; Feteira, A.; Jackson, T.; Reichmann, K., Lone-Pair-Induced Covalency as the Cause of Temperature- and Field-Induced Instabilities in Bismuth Sodium Titanate. *Adv. Funct. Mater.* **2012,** *22*, 2285-2294.

(6) Keeble, D. S.; Barney, E. R.; Keen, D. A.; Tucker, M. G.; Kreisel, J.; Thomas, P. A., Bifurcated Polarization Rotation in Bismuth-Based Piezoelectrics. *Adv. Funct. Mater.* **2013,** *23*, 185-190.

(7) Smolenskii, G. A.; Isupov, V. A.; Agranovskaya, A. I.; Krainik, N. N., New ferroelectrics of a complex composition: 4. *Sov. Phys. Solid State* **1961,** *2*, 2651-2654.

(8) Wefring, E. T.; Einarsrud, M. A.; Grande, T., Electrical conductivity and thermopower of $(1-x)BiFeO_3$ - $xBi_{0.5}K_{0.5}TiO_3$ (x = 0.1, 0.2) ceramics near the ferroelectric to paraelectric phase transition. *Phys. Chem. Chem. Phys.* **2015,** *17*, 9420-9428.

(9) Wefring, E. T.; Schader, F. H.; Webber, K. G.; Einarsrud, M. A.; Grande, T., Electrical conductivity and ferroelastic properties of Ti-substituted solid solutions $(1-x)BiFeO_3$ - $xBi_{0.5}K_{0.5}TiO_3$. *J. Eur. Ceram. Soc.* **2016,** *36*, 497-506.

(10) Matsuo, H., Ferroelectric Properties and Domain Structures of $(Bi_{0.5}K_{0.5})TiO_3$-$BiFeO_3$ Ceramics.pdf. *Trans. Mat. Res. Soc. Japan* **2011,** *2*, 285-288.

(11) Ozaki, T.; Matsuo, H.; Noguchi, Y.; Miyayama, M.; Mori, S., Microstructures Related to Ferroelectric Properties in $(Bi_{0.5}K_{0.5})TiO_3$–$BiFeO_3$. *Jpn. J. Appl. Phys.* **2010,** *49*, 09MC05.
(12) Morozov, M. I.; Einarsrud, M.-A.; Grande, T., Atmosphere controlled conductivity and Maxwell-Wagner relaxation in $Bi_{0.5}K_{0.5}TiO_3$–$BiFeO_3$ ceramics. *J. Appl. Phys.* **2014,** *115*, 044104.
(13) Morozov, M. I.; Einarsrud, M.-A.; Grande, T., Control of conductivity and electric field induced strain in bulk $Bi_{0.5}K_{0.5}TiO_3$–$BiFeO_3$ ceramics. *Appl. Phys. Lett.* **2014,** *104*, 122905.
(14) Morozov, M. I.; Einarsrud, M.-A.; Grande, T., Polarization and strain response in $Bi_{0.5}K_{0.5}TiO_3$-$BiFeO_3$ ceramics. *Appl. Phys. Lett.* **2012,** *101*, 252904.
(15) Morozov, M. I.; Einarsrud, M. A.; Grande, T.; Damjanovic, D., Lead-Free Relaxor-Like $0.75Bi_{0.5}K_{0.5}TiO_3$ –$0.25BiFeO_3$ Ceramics with Large Electric Field-Induced Strain. *Ferroelectrics* **2012,** *439*, 88-94.
(16) Hiruma, Y.; Aoyagi, R.; Nagata, H.; Takenaka, T., Ferroelectric and Piezoelectric Properties of $(Bi_{1/2}K_{1/2})TiO_3$ Ceramics. *Jpn. J. Appl. Phys.* **2005,** *44*, 5040-5044.
(17) Wefring, E. T.; Morozov, M. I.; Einarsrud, M.-A.; Grande, T.; Trolier-McKinstry, S. E., Solid-State Synthesis and Properties of Relaxor (1−x)BKT-xBNZ Ceramics. *J. Am. Ceram. Soc.* **2014,** *97*, 2928-2935.
(18) Hiruma, Y.; Nagata, H.; Takenaka, T., Grain-size effect on electrical properties of $(Bi_{1/2}K_{1/2})TiO_3$ ceramics. *Jpn. J. Appl. Phys.* **2007,** *46*, 1081-1084.
(19) Burns, G.; Dacol, F. H., Glassy polarisation behaviour in ferroelectric compounds $Pb(Mg_{1/3}Nb_{2/3})O_3$ and $Pb(Zn_{1/3}Nb_{2/3})O_3$. *Solid State Commun.* **1983,** *48*, 853-856.
(20) Otonicar, M.; Skapin, S. D.; Spreitzer, M.; Suvorov, D., Compositional range and electrical properties of the morphotropic phase boundary in the Na0.5Bi0.5TiO3-K0.5Bi0.5TiO3 system. *J. Eur. Ceram. Soc.* **2010,** *30*, 971-979.
(21) Ivanova, V. V., Kapyshev, A.G., Venevtsev, Yu.N., Zhdanov, G.S., X-ray determination of the symmetry of the ferroelectric compounds (potassium or sodium) (0.5) bismuthi (0.5) titanate and the high temperature phase transitions in potassium (0.5) bismuth (0.5) titanate. *Bull. Acad. Sci. USSR Phys. Ser.* **1962,** *26*, 358-360.
(22) Otonicar, M.; Skapin, S. D.; Jancar, B.; Ubic, R.; Suvorov, D., Analysis of the phase transition and the domain structure in $K_{0.5}Bi_{0.5}TiO_3$ perovskite ceramics by in situ XRD and TEM. *J. Am. Ceram. Soc.* **2010,** *93*, 4168-4173.
(23) Hagiwara, M.; Fujihara, S., Grain size effect on phase transition behavior and electrical properties of $(Bi_{1/2}K_{1/2})TiO_3$ piezoelectric ceramics. *Jpn. J. Appl. Phys.* **2015,** *54*, 10ND10.
(24) Yang, J. F.; Hou, Y. D.; Wang, C.; Zhu, M. K.; Yan, H., Relaxor behavior of $(K_{0.5}Bi_{0.5})TiO_3$ ceramics derived from molten salt synthesized single-crystalline nanowires. *Appl. Phys. Lett.* **2007,** *91*, 023118.
(25) Li, Z. F.; Wang, C. L.; Zhong, W. L.; Li, J. C.; Zhao, M. L., Dielectric relaxor properties of $K_{0.5}Bi_{0.5}TiO_3$ ferroelectrics prepared by sol-gel method. *J. Appl. Phys.* **2003,** *94*, 2548-2552.
(26) Li, F.; Zhang, S. J.; Xu, Z.; Chen, L. Q., The Contributions of Polar Nanoregions to the Dielectric and Piezoelectric Responses in Domain-Engineered Relaxor-$PbTiO_3$ Crystals. *Adv. Funct. Mater.* **2017,** *27*, 1700310.
(27) Kim, Y. M.; Morozovska, A.; Eliseev, E.; Oxley, M. P.; Mishra, R.; Selbach, S. M.; Grande, T.; Pantelides, S. T.; Kalinin, S. V.; Borisevich, A. Y., Direct observation of ferroelectric field effect and vacancy-controlled screening at the $BiFeO_3/La_xSr_{1-x}MnO_3$ interface. *Nat. Mater.* **2014,** *13*, 1019-1025.
(28) Macutkevic, J.; Banys, J.; Bussmann-Holder, A.; Bishop, A. R., Origin of polar nanoregions in relaxor ferroelectrics: Nonlinearity, discrete breather formation, and charge transfer. *Phys. Rev. B* **2011,** *83*, 184301

(29) Hagiwara, M.; Fujihara, S., Grain-size-dependent spontaneous relaxor-to-ferroelectric phase transition in $(Bi_{1/2}K_{1/2})TiO_3$ ceramics. *Appl. Phys. Lett.* **2015,** *107*, 012903.
(30) Jones, G. O.; Kreisel, J.; Thomas, P. A., A structural study of the $(Na_{1-x}K_x)_{0.5}Bi_{0.5}TiO_3$ perovskite series as a function of substitution ($x$) and temperature. *Powder Diffr.* **2002,** *17*, 301-319.
(31) King, G.; Woodward, P. M., Cation ordering in perovskites. *J. Mater. Chem.* **2010,** *20*, 5785-5796.
(32) Shannon, R. D., Revised effective ionic-radii and systematic studies of interatomic distances in halides and chalcogenides. *Acta Crystallogr., Sect. A* **1976,** *32*, 751-767.
(33) Jiang, B.; Grande, T.; Selbach, S. M., Local Structure of Disordered $Bi_{0.5}K_{0.5}TiO_3$ Investigated by Pair Distribution Function Analysis and First-Principles Calculations. *Chem. Mater.* **2017,** *29*, 4244-4252.
(34) Aksel, E.; Forrester, J. S.; Nino, J. C.; Page, K.; Shoemaker, D. P.; Jones, J. L., Local atomic structure deviation from average structure of $Na_{0.5}Bi_{0.5}TiO_3$: Combined x-ray and neutron total scattering study. *Phys. Rev. B* **2013,** *87*, 104113.
(35) Shuvaeva, V. A.; Zekria, D.; Glazer, A. M.; Jiang, Q.; Weber, S. M.; Bhattacharya, P.; Thomas, P. A., Local structure of the lead-free relaxor ferroelectric$(K_xNa_{1-x})_{0.5}Bi_{0.5}TiO_3$. *Phys. Rev. B* **2005,** *71*, 174114.
(36) Petkov, V., Nanostructure by high-energy X-ray diffraction. *Mater. Today* **2008,** *11*, 28-38.
(37) Petkov, V.; Selbach, S. M.; Einarsrud, M. A.; Grande, T.; Shastri, S. D., Melting of Bi Sublattice in Nanosized $BiFeO_3$ Perovskite by Resonant X-Ray Diffraction. *Phys. Rev. Lett.* **2010,** *105*, 185501.
(38) Liu, H.; Chen, J.; Fan, L. L.; Ren, Y.; Pan, Z.; Lalitha, K. V.; Rodel, J. G.; Xing, X. R., Critical Role of Monoclinic Polarization Rotation in High-Performance Perovskite Piezoelectric Materials. *Phys. Rev. Lett.* **2017,** *119*, 017601.
(39) Liu, H.; Chen, J.; Fan, L. L.; Ren, Y.; Hu, L.; Guo, F. M.; Deng, J. X.; Xing, X. R., Structural Evidence for Strong Coupling between Polarization Rotation and Lattice Strain in Monoclinic Relaxor Ferroelectrics. *Chem. Mater.* **2017,** *29*, 5767-5771.
(40) Young, C. A.; Goodwin, A. L., Applications of pair distribution function methods to contemporary problems in materials chemistry. *J. Mater. Chem.* **2011,** *21*, 6464-6476.
(41) Keen, D. A.; Goodwin, A. L., The crystallography of correlated disorder. *Nature* **2015,** *521*, 303-309.
(42) Hou, D.; Zhao, C.; Paterson, A. R.; Li, S.; Jones, J. L., Local structures of perovskite dielectrics and ferroelectrics via pair distribution function analyses. *J. Eur. Ceram. Soc. 38*, 971-987.
(43) Jeong, I. K.; Darling, T. W.; Lee, J. K.; Proffen, T.; Heffner, R. H.; Park, J. S.; Hong, K. S.; Dmowski, W.; Egami, T., Direct observation of the formation of polar nanoregions in $Pb(Mg_{1/3}Nb_{2/3})O_3$ using neutron pair distribution function analysis. *Phys. Rev. Lett.* **2005,** *94*, 147602.
(44) Billinge, S. J. L.; Levin, I., The problem with determining atomic structure at the nanoscale. *Science* **2007,** *316*, 561-565.
(45) Fu, H. X.; Cohen, R. E., Polarization rotation mechanism for ultrahigh electromechanical response in single-crystal piezoelectrics. *Nature* **2000,** *403*, 281-283.
(46) Tse, J. S., Ab initio molecular dynamics with density functional theory. *Annu. Rev. Phys. Chem.* **2002,** *53*, 249-290.
(47) Larson, A. C.; Dreele, R. B. V., General Structure Analysis System technical manual. *LANSCE, MS–H805 Los Almos National Laboratory LAUR* **2000**, 86-748.

(48) Juhas, P.; Davis, T.; Farrow, C. L.; Billinge, S. J. L., PDFgetX3: a rapid and highly automatable program for processing powder diffraction data into total scattering pair distribution functions. *J. Appl. Crystallogr.* **2013,** *46*, 560-566.
(49) Farrow, C. L.; Juhas, P.; Liu, J. W.; Bryndin, D.; Bozin, E. S.; Bloch, J.; Proffen, T.; Billinge, S. J., PDFfit2 and PDFgui: computer programs for studying nanostructure in crystals. *J. Phys. Condens. Matter* **2007,** *19*, 335219.
(50) Tucker, M. G.; Keen, D. A.; Dove, M. T.; Goodwin, A. L.; Hui, Q., RMCProfile: reverse Monte Carlo for polycrystalline materials. *J. Phys. Condens. Matter* **2007,** *19*, 335218.
(51) Kresse, G.; Furthmuller, J., Efficient iterative schemes for ab initio total-energy calculations using a plane-wave basis set. *Phys. Rev. B* **1996,** *54*, 11169-11186.
(52) Kresse, G.; Joubert, D., From ultrasoft pseudopotentials to the projector augmented-wave method. *Phys. Rev. B* **1999,** *59*, 1758-1775.
(53) Perdew, J. P.; Ruzsinszky, A.; Csonka, G. I.; Vydrov, O. A.; Scuseria, G. E.; Constantin, L. A.; Zhou, X. L.; Burke, K., Restoring the density-gradient expansion for exchange in solids and surfaces. *Phys. Rev. Lett.* **2008,** *100*, 136406.
(54) Perdew, J. P.; Burke, K.; Ernzerhof, M., Generalized gradient approximation made simple. *Phys. Rev. Lett.* **1996,** *77*, 3865-3868.
(55) Gröting, M.; Hayn, S.; Albe, K., Chemical order and local structure of the lead-free relaxor ferroelectric. *J. Solid State Chem.* **2011,** *184*, 2041-2046.
(56) Gröting, M.; Albe, K., Comparative study of A-site order in the lead-free bismuth titanates M1/2Bi1/2TiO3 (M=Li, Na, K, Rb, Cs, Ag, Tl) from first-principles. *J. Solid State Chem.* **2014,** *213*, 138-144.
(57) Windiks, R.; Delley, B., Massive thermostatting in isothermal density functional molecular dynamics simulations. *J. Chem. Phys.* **2003,** *119*, 2481-2487.
(58) Nose, S., A unified formulation of the constant temperature molecular-dynamics methods. *J. Chem. Phys.* **1984,** *81*, 511-519.
(59) Zhang, Q. S.; Cagin, T.; Goddard, W. A., The ferroelectric and cubic phases in $BaTiO_3$ ferroelectrics are also antiferroelectric. *Proc. Natl. Acad. Sci. U.S.A.* **2006,** *103*, 14695-14700.
(60) Senn, M. S.; Keen, D. A.; Lucas, T. C. A.; Hriljac, J. A.; Goodwin, A. L., Emergence of Long-Range Order in $BaTiO_3$ from Local Symmetry-Breaking Distortions. *Phys. Rev. Lett.* **2016,** *116*, 207602.
(61) Smith, M. B.; Page, K.; Siegrist, T.; Redmond, P. L.; Walter, E. C.; Seshadri, R.; Brus, L. E.; Steigerwald, M. L., Crystal structure and the paraelectric-to-ferroelectric phase transition of nanoscale $BaTiO_3$. *J. Am. Chem. Soc.* **2008,** *130*, 6955-6963.
(62) Petkov, V.; Buscaglia, V.; Buscaglia, M.; Zhao, Z.; Ren, Y., Structural coherence and ferroelectricity decay in submicron- and nano-sized perovskites. *Phys. Rev. B* **2008,** *78*, 054107.
(63) Page, K.; Proffen, T.; Niederberger, M.; Seshadri, R., Probing Local Dipoles and Ligand Structure in $BaTiO_3$ Nanoparticles. *Chem. Mater.* **2010,** *22*, 4386-4391.
(64) Jeong, I. K., Temperature evolution of short- and medium-range ionic correlations in relaxor ferroelectric $[Pb(Zn_{1/3}Nb_{2/3})O_3]_{(1-x)}$ $[PbTiO_3]_x$ (x=0.05, 0.12). *Phys. Rev. B* **2009,** *79*, 052101

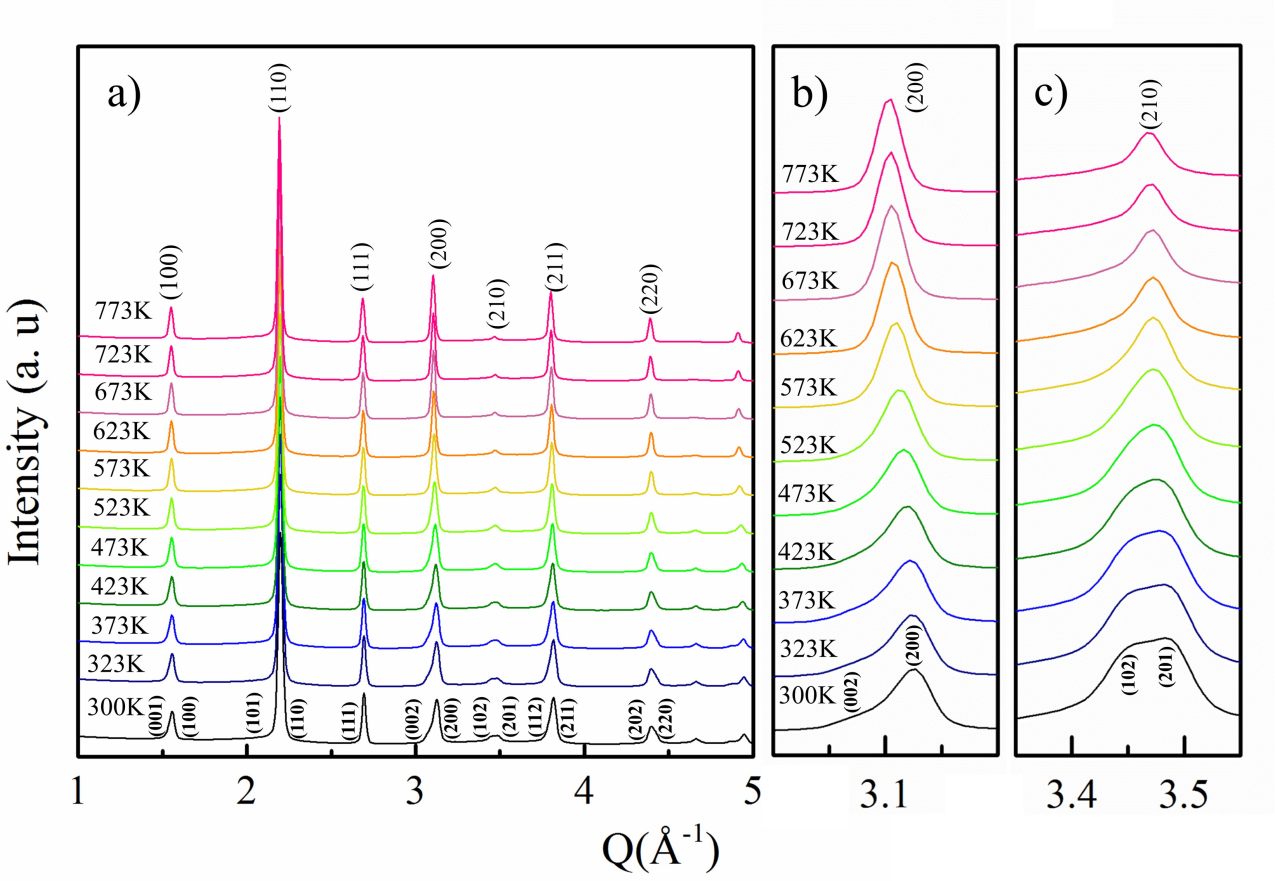


Figure 1. (a) X-ray patterns of BKT from room temperature to 773 K in intervals of 50K. Reflections were indexed as tetragonal at RT and cubic at 773K. (b-c) shows the $(200)_c$ and $(210)_c$ reflections, respectively. Subscript c denotes cubic.

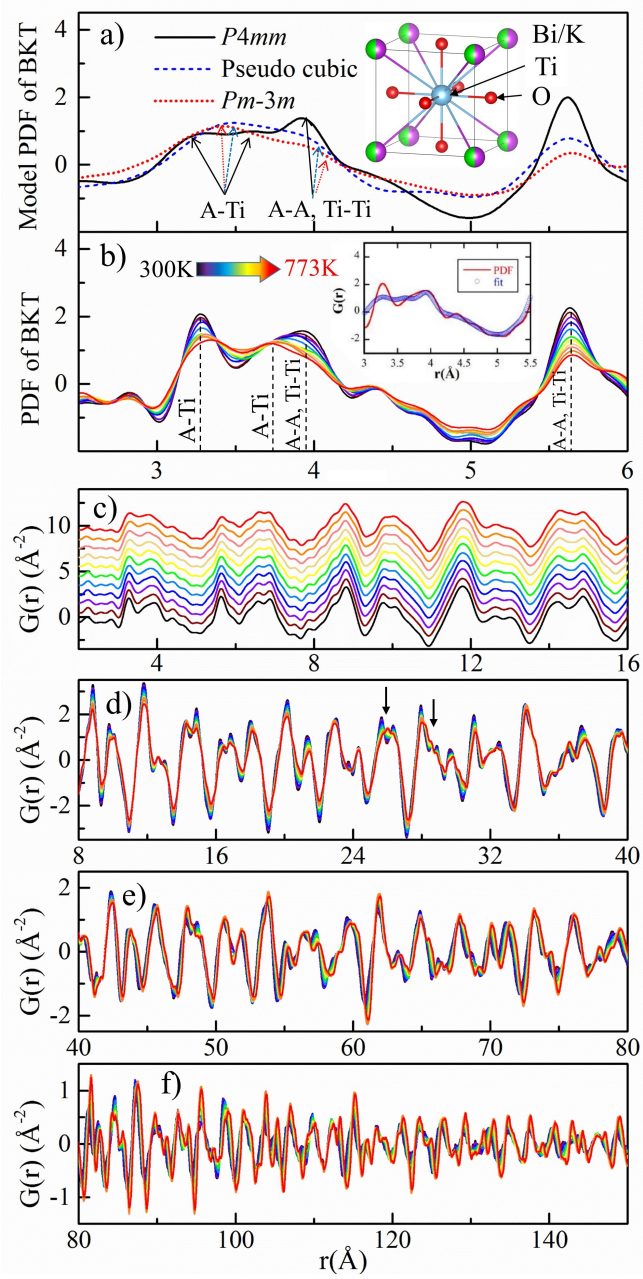


Figure 2. Pair distribution functions (PDF) of $Bi_{0.5}K_{0.5}TiO_3$ (BKT). a) Simulated PDFs of average structure models with randomly occupied A-sites with *P*4*mm*, pseudo-cubic and *Pm* $\bar{3}$ *m* lattices. The inset shows the mixed A-site *P*4*mm* perovskite structure. b) Measured temperature dependent PDF patterns from room temperature (black) to 773 K (red). Inset: Experimental PDF at 300K and simulated PDF for mixed A-site *P*4*mm*. c) Local and intermediate range PDF patterns for BKT from room temperature (black) to 773 K (red), the PDF patterns are shifted along the y-axis for clarity. (d-f) shows the temperature dependence of PDF patterns for different r-ranges up to r = 150 Å.

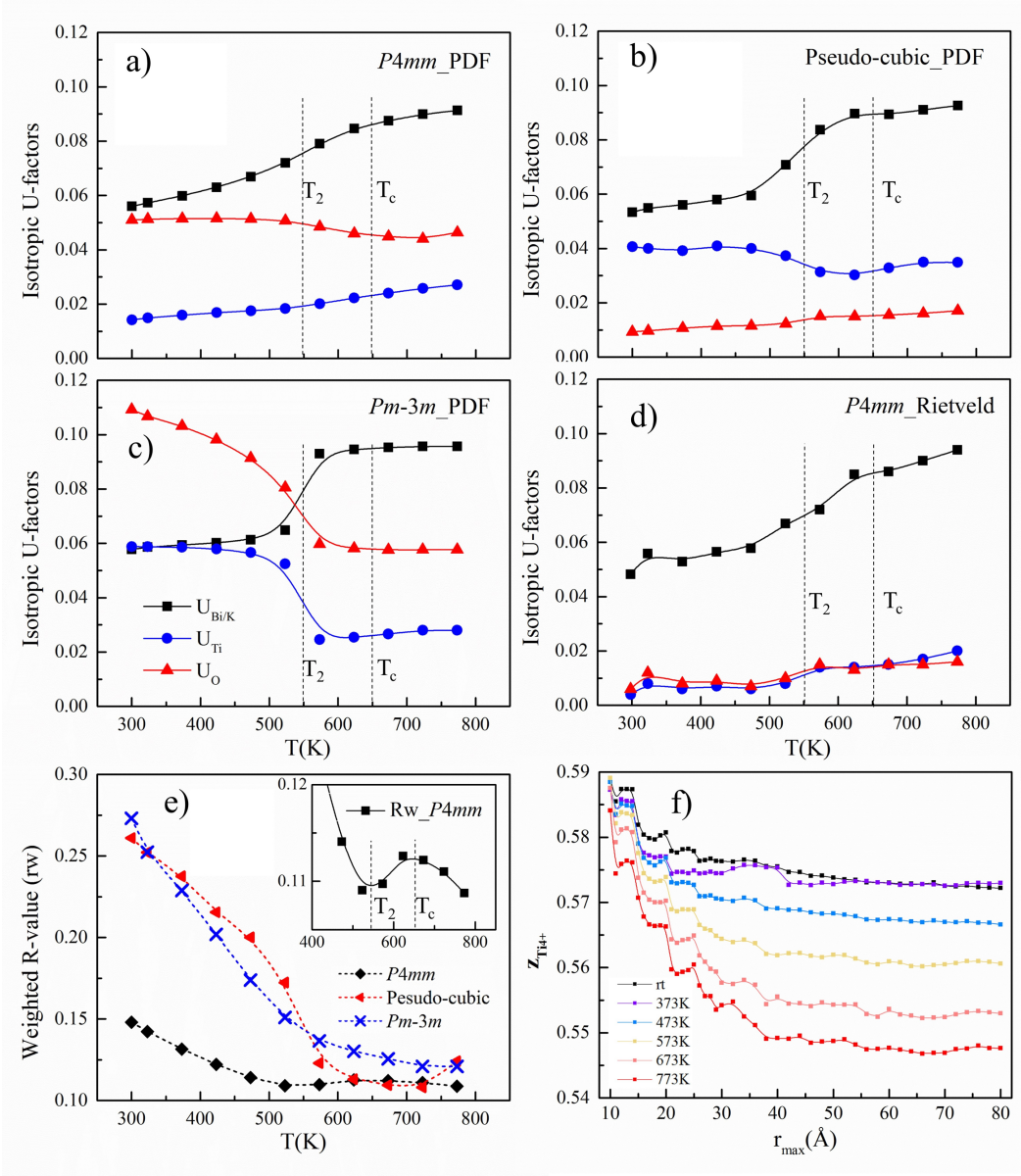


Figure 3. Temperature dependent isotropic atomic displacement factors *U* from PDFs refined from r = 1.5 Å to 80 Å with (a) *P*4*mm*, (b) pseudo-cubic and (c) $Pm\bar{3}m$ models, and (d) *P*4*mm* model from Rietveld refinement. (e) Weighted reliability factors ($R_w$) for PDF refinements. The inset shows the $R_w$ for the *P*4*mm* model across $T_2$ and $T_C$. The phase transition temperatures $T_2$ (~550K) and $T_C$ (~650K) are indicated as vertical dotted lines. (f) $Ti^{4+}$ displacement from PDF with varying $r_{max}$ from 10 Å to 80 Å and $r_{min}$ fixed to 1.5 Å. The scale factor, $Q_{damp}$ and lattice constants *a* and *c* were fixed to the values refined for $r_{max}$ = 80 Å for all other values of $r_{max}$.

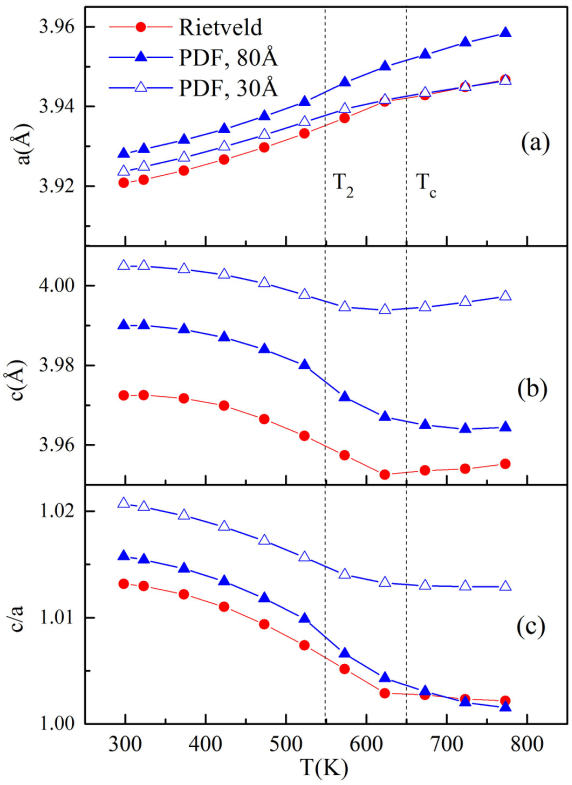


Figure 4. Temperature dependent local and average unit cell parameters of $Bi_{0.5}K_{0.5}TiO_3$. (a-b) Lattice parameters *a* and *c*, and (c) tetragonality *c*/*a* from Rietveld refinement and PDF refinement over *r* ranges of 80 Å and 30 Å. The phase transition temperatures $T_2$ (~550K) and $T_C$ (~650K) are depicted as vertical dotted lines.

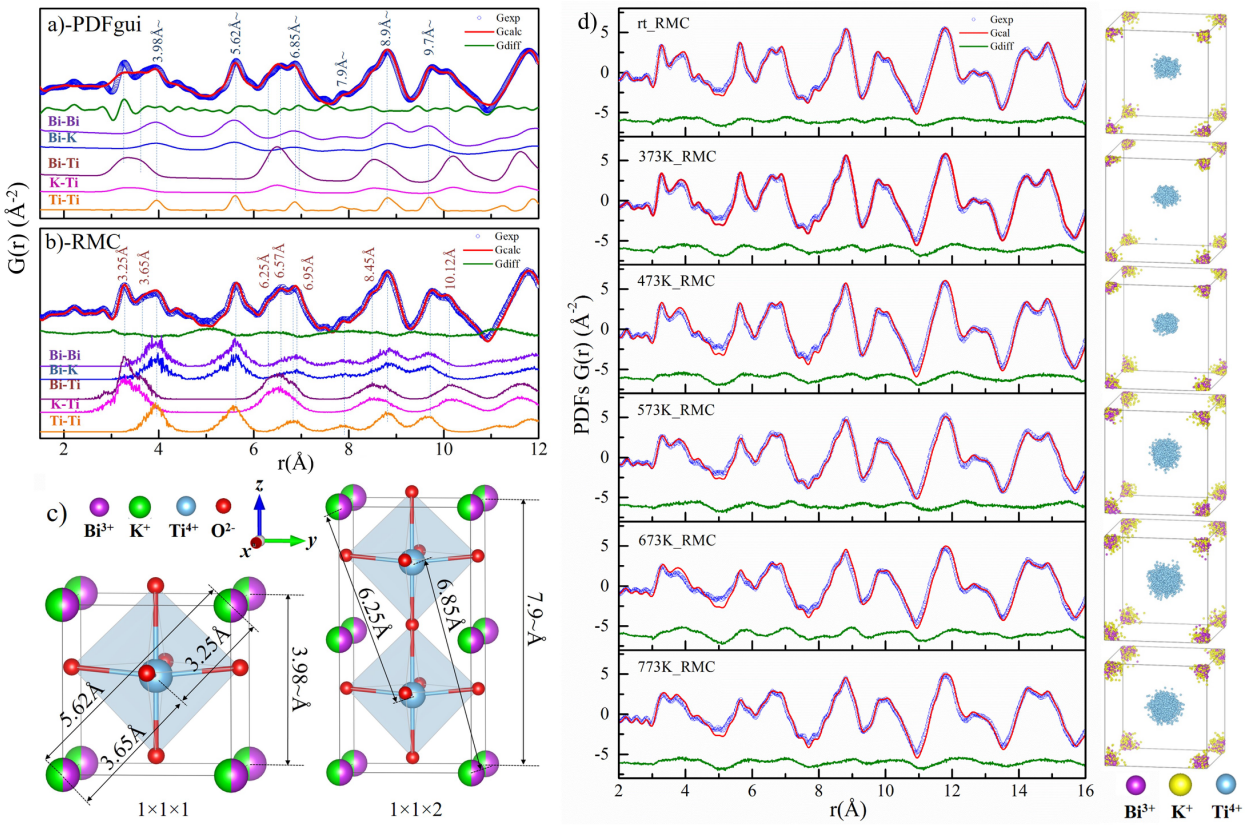


Figure 5. Experimental PDF and simulated total and partial PDFs of $Bi_{0.5}K_{0.5}TiO_3$. a) Room temperature PDF and partial PDFs simulated with the mixed A-site *P*4*mm* model. b) Experimental PDF and RMC simulated total and partial PDFs using 12×12×12 *P*4*mm* supercells. c) 1×1×1 and 1×1×2 *P*4*mm* mixed A-site model supercell with interatomic distances shown. d) RMC simulated PDFs and experimental PDFs collected at selected temperatures. Open circles: experimental data; red solid lines: calculated data; green lines: difference curves. Cation distribution clouds for $Bi^{3+}$, $K^+$ and $Ti^{4+}$ are shown next to the PDFs.

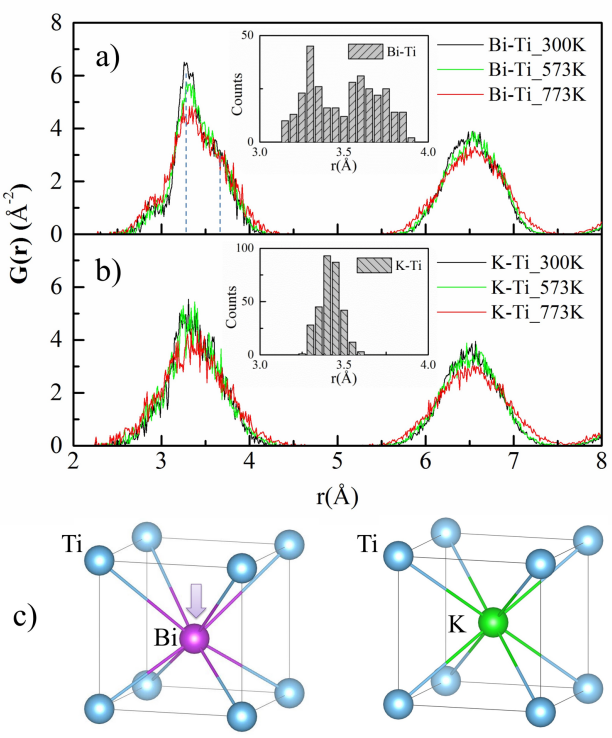


Figure 6. Partial PDFs of $Bi_{0.5}K_{0.5}TiO_3$ showing a) Bi-Ti and b) K-Ti bond lengths in $Bi_{0.5}K_{0.5}TiO_3$ from RMC simulations at 300K, 573K and 773K, corresponding to tetragonal *P*4*mm*, pseudo-cubic and *Pm* $\overline{3}$ *m* ideal cubic structures. Insets show the statistical distribution of Bi-Ti and K-Ti bond lengths obtained by the different A-site configurations after geometry optimization by DFT. c) Cation coordination polyhedra for Bi-Ti and K-Ti in BKT.

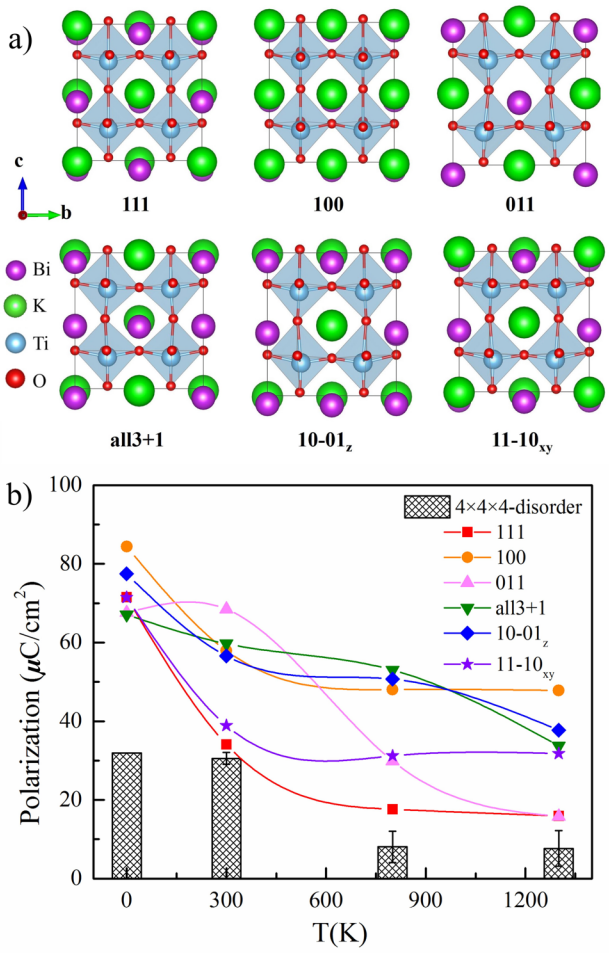


Figure 7. a) Different A-site configurations of $Bi_{0.5}K_{0.5}TiO_3$ after geometry optimization by DFT at 0K. b) Point charge model calculated polarization ($P_s$) of randomly selected 4×4×4 disordered supercells (grey bar area) and six different configurations at 0, 300, 800 and 1300K.

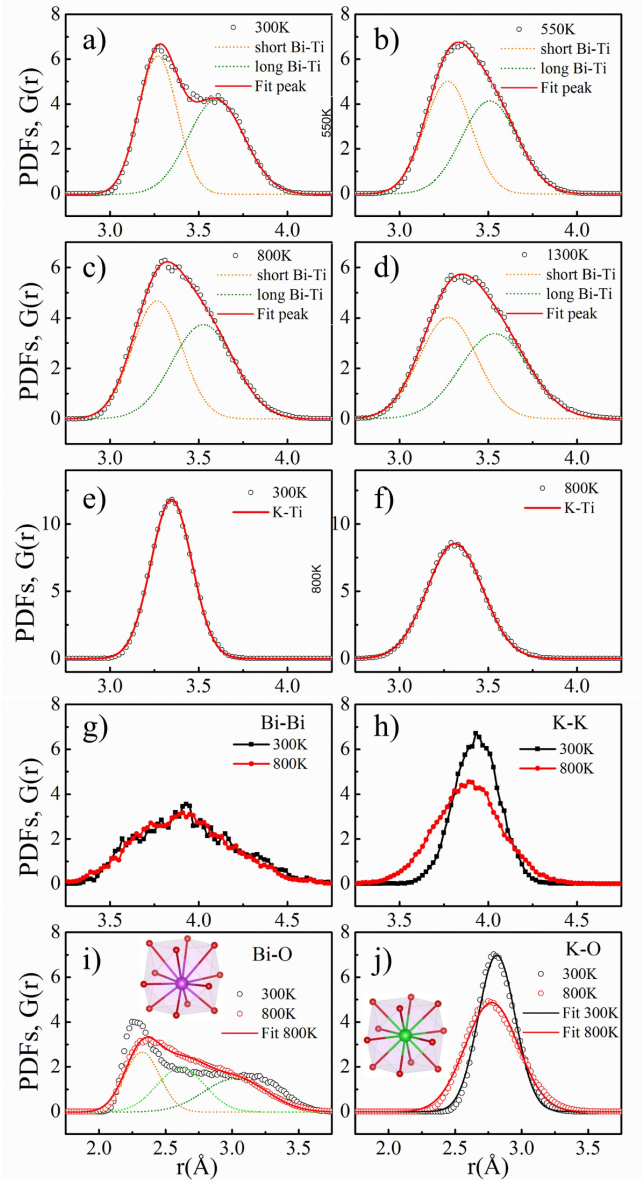


Figure 8. Radial distribution functions from ab initio molecular dynamics (AIMD) simulations of $Bi_{0.5}K_{0.5}TiO_3$. a)-d) Bi-Ti radial pair distribution functions g(r) from AIMD and equal area deconvoluted Gaussian peaks at different temperatures. e)-f) K-Ti radial pair distribution functions g(r) from AIMD fitted to single peaks. Radial pair distribution function g(r) from AIMD at 300K and 800K for g) Bi-Bi, h) K-K, i) Bi-O and j) K-O. Deconvoluted Gaussian peaks used three equal areas for the Bi-O bond distribution peaks at 800K, and single peak for the K-O bond distribution.

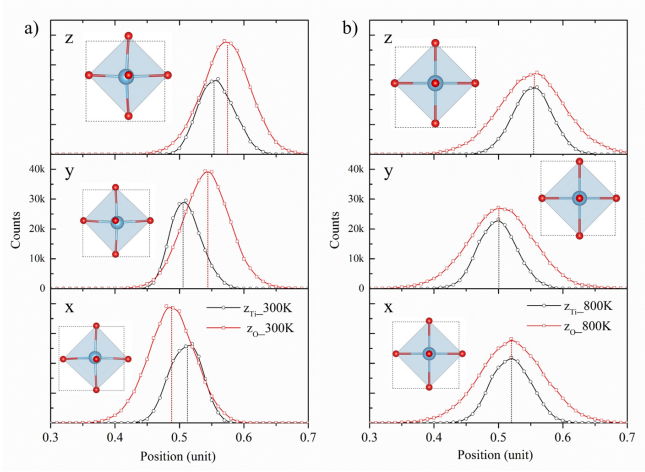


Figure 9. Distributions of $Ti^{4+}$ and $O^{2-}$ positions at (a) 300K and (b) 800K in the unit cell relative to the average $TiO_6$ octahedron. Dashed vertical lines give the average values for each peak. The *x*, *y* and *z* directions are along the *a*, *b* and *c* unit cell axes, respectively.

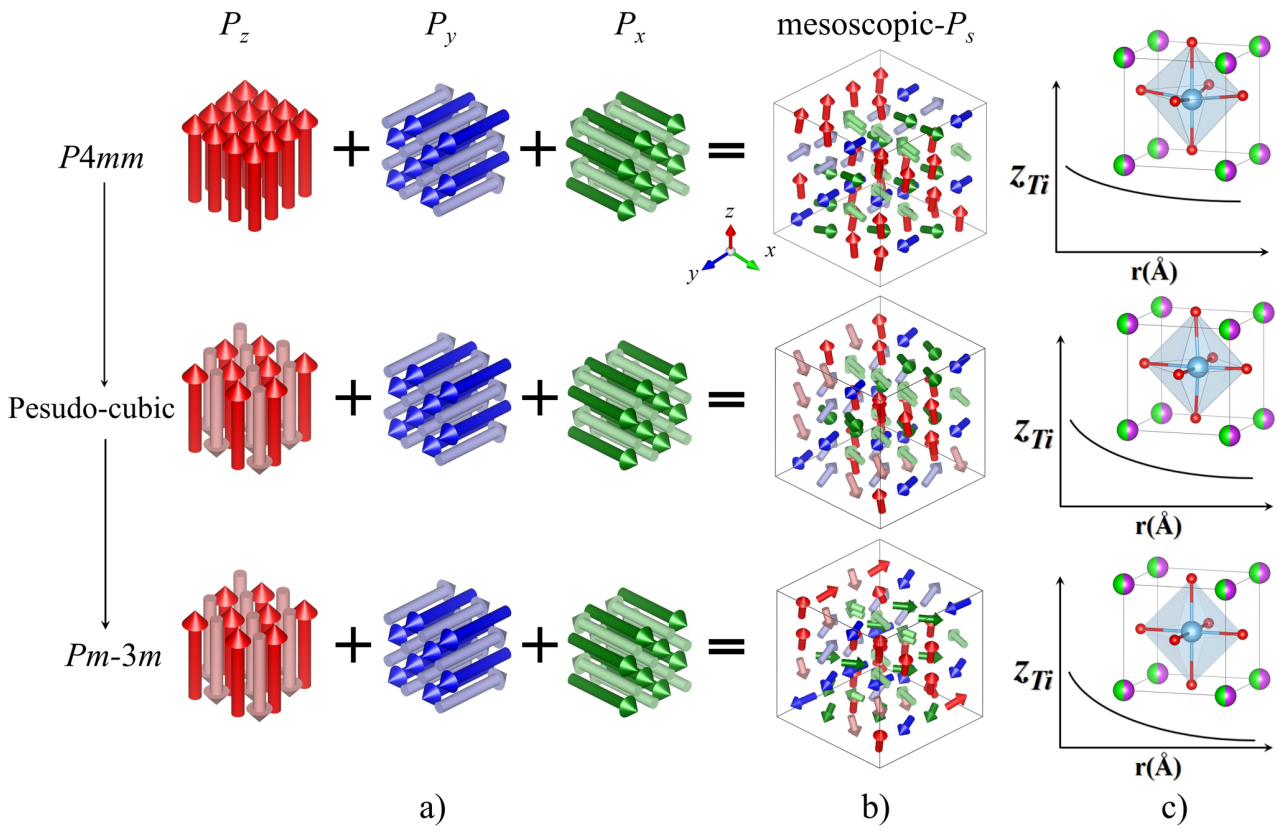


Figure 10. Local structure and order-disorder phase transition in BKT. a) Arrows depict the polarization directions of microscopic polar regions. b) Proposed 3D mesoscopic structure model of BKT for the different phases. c) Schematic illustration of how the spatially averaged $Ti^{4+}$ displacement depends on the radius *r* of a sphere of BKT considered for each phase.